

Near-infrared-to-visible photon upconversion process induced by exchange interactions in Yb^{3+} -doped RbMnCl_3

Rafael Valiente, Oliver S. Wenger, and Hans U. Güdel*

Department of Chemistry and Biochemistry, University of Bern, Freiestrasse 3, CH-3000 Bern 9, Switzerland

(Received 19 September 2000; revised manuscript received 18 December 2000; published 2 April 2001)

Crystals of RbMnCl_3 doped with Yb^{3+} exhibit a strong orange luminescence under near-infrared Yb^{3+} excitation at 10 K. The broad emission band extending from $17\,200\text{ cm}^{-1}$ to $13\,000\text{ cm}^{-1}$ is identified as a ${}^4T_1 \rightarrow {}^6A_1$ transition on Mn^{2+} . Of the two inequivalent Yb^{3+} sites identified by site-selective high-resolution spectroscopy, only one is able to induce efficient upconversion. Excitation with 10-ns pulses indicates that no energy transfer is involved, and the upconversion process consists of a sequence of ground-state absorption and excited-state absorption steps. One- and two-color excitation spectra confirm the occurrence of these two steps. The efficiency of the upconversion process at 10 K and for an excitation power of 200 mW focused by a 53-mm lens is 2 percent. An upconversion mechanism based on exchange interactions between the Yb^{3+} and Mn^{2+} ions is proposed to account for the observed behavior.

DOI: 10.1103/PhysRevB.63.165102

PACS number(s): 78.55.Hx, 75.30.Et, 78.47.+p

I. INTRODUCTION

Photon upconversion (UC) phenomena and UC materials have been studied and described in the literature since the early work of Auzel in 1966.¹ Most of the work has been devoted to rare-earth ions doped into crystals and glasses. The research objectives have been both fundamental, trying to understand and model the underlying mechanisms, and oriented towards photonic applications. About ten years ago the idea of creating blue and green lasers based on upconversion from the near infrared (NIR) was pursued quite vigorously. With the advent of semiconductor diode lasers in this spectral range, this activity has been significantly reduced. Exciting lighting or display phosphors by upconversion remains a challenging and interesting possibility, and there is still significant research activity in this area.

At least two metastable excited states have to be present for a material to exhibit upconversion. f - f excited states in lanthanides are often metastable due to the reduced electron-phonon coupling by the shielded f electrons. Multiple metastable excited states in transition metal ion systems are much less common, because multiphonon relaxation processes are more dominant. And until recently, no systematic upconversion studies on transition metal ion systems were reported. Upconversion processes have so far been found to occur in Ti^{2+} ,² Ni^{2+} ,³ Mo^{3+} ,⁴ Re^{4+} ,⁵ and Os^{4+} (Ref. 6) doped halide lattices. The combination of transition metal and lanthanide ions should open up new pathways and mechanisms for upconversion processes. Crystals codoped with transition metal and lanthanide ions have been studied for a long time. But their importance, e.g., in the laser crystal yttrium aluminum garnet (YAG): Nd^{3+} , Cr^{3+} ,⁷ lies in the ability of the transition metal ion to act as a sensitizer for the lanthanide activator. The present study has a completely different objective, which has not been investigated so far. Both the transition metal and the lanthanide ion are active partners in a new type of upconversion process.

In Figs. 1(a)–1(d), we schematically summarize the estab-

lished upconversion mechanisms relevant as a basis and for a discussion of the present paper:

(1a) Ground-state absorption/excited-state absorption (GSA/ESA) or upconversion by two-step absorption. An ion excited via GSA is promoted to an upper emitting state by ESA of a second photon. This process is *basically* a single-ion process and exhibits an instantaneous rise of the UC luminescence by a short excitation pulse, because both GSA and ESA steps have to occur within the duration of the laser pulse.

(1b) GSA/ETU or energy-transfer upconversion.¹ Two ions excited to the intermediate level by GSA interact via a nonradiative energy-transfer process to generate one ion in the upper-excited state and the other one in the ground state. Being a nonradiative process, ETU can proceed after the pulse, and this is identified as a rise in the upconversion luminescence after a short laser pulse preceding its decay.

(1c) Cooperative sensitization. Two excited donor ions simultaneously transfer their excitation energy to the acceptor ion, which has no energy level close to the excited state of the donor.⁸ This three-ion process may become relevant when the donor ions tend to dimerize or when the donor

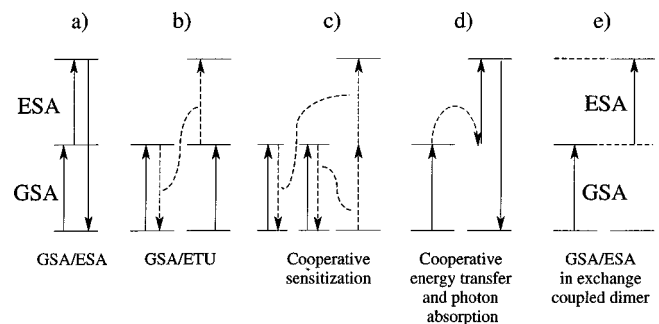


FIG. 1. Schematic representation of photon upconversion mechanisms. GSA denotes ground-state absorption and ESA excited-state absorption. The full arrow lines represent radiative transitions and dashed lines represent nonradiative processes.

excitation is mobile. Its temporal behavior is expected to be similar to the GSA/ETU, because it also involves a slow energy-transfer step.

(1d) Cooperative energy transfer and photon absorption. An excited donor ion transfers its energy to an acceptor while the acceptor simultaneously absorbs a photon.⁹ This process is expected to have an instantaneous buildup after the laser pulse.

It will be shown and discussed in detail in Sec. IV D that none of these mechanisms can account for the new phenomenon. A new mechanism based on exchange interactions between the Yb^{3+} ion and a neighboring Mn^{2+} is postulated.¹⁰ This is schematically shown for an Yb^{3+} - Mn^{2+} pair in Fig. 1(e).

In a recent letter we published results of a potentially very efficient NIR to visible (VIS) UC process, which is induced by the combination of a transition metal (Mn^{2+}) and a lanthanide ion (Yb^{3+}) in a single-crystal lattice.¹¹ Now we present a more complete account of the experimental results and suggest possible mechanisms for the UC process for $\text{RbMnCl}_3:\text{Yb}^{3+}$. Excitation into the Yb^{3+} absorption levels around $1 \mu\text{m}$ leads to visible Mn^{2+} 4T_1 emission. Several experiments have been designed to determine and clarify the UC mechanism in $\text{RbMnCl}_3:\text{Yb}^{3+}$.

II. EXPERIMENT

A. Crystal growth and manipulation

Single crystals of Yb^{3+} -doped RbMnCl_3 were grown by the Bridgman technique using stoichiometric amounts of RbCl and MnCl_2 and a trace of YbCl_3 , as described elsewhere.¹² Crystals of centimeter dimensions were obtained with excellent optical quality. The actual ytterbium concentration in the crystals determined by inductively coupled plasma mass spectrometry measurements was 0.08 mol %. This method cannot distinguish between different valence states, and therefore, the actual Yb^{3+} concentration in the crystal is slightly smaller, as we have spectroscopic evidence for the presence of Yb^{2+} . Crystals were selected and oriented with a polarizing microscope. They were cut using a diamond saw and polished for absorption measurements. Due to the hygroscopic nature of the starting materials and the crystals, all the handling was carried out under a dry inert atmosphere. The crystals were mounted in a closed copper cell or closed quartz ampoules filled with He gas for absorption and emission measurements, respectively. Sample cooling was achieved using a closed-cycle cryostat (Air Products) for absorption measurements or a quartz He flow-tube for luminescence measurements.

B. Spectroscopic measurements

Polarized absorption spectra were measured on a Cary 5E (Varian) spectrometer with $\mathbf{E}\parallel\mathbf{c}(\pi)$ and $\mathbf{E}\perp\mathbf{c}(\sigma)$ where c is the unique axis of the hexagonal RbMnCl_3 crystals. The crystal thickness for Yb^{3+} absorption spectroscopy was about 1.35 cm. Upconversion luminescence was excited by an Ar^+ ion laser (Spectra Physics 2060-10 SA) pumped tun-

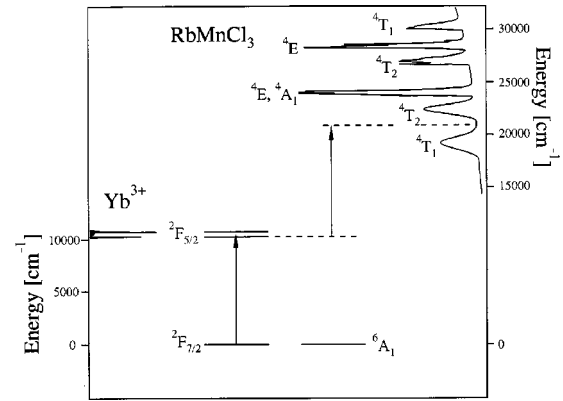


FIG. 2. Absorption spectra of RbMnCl_3 (right) and Yb^{3+} doped RbMnCl_3 (left) single crystals at 11 K. The one-color upconversion excitation scheme is shown in the center.

able Ti: sapphire laser (Spectra Physics 3900S). The emission was dispersed by a 0.85 m double monochromator (Spex 1402) using 500 nm blazed 1200 grooves/mm gratings and detected by a cooled photomultiplier (RCA C31034 or Hamamatsu 3310-01) and a photon-counting system (Stanford Research SR400). Downconversion Mn^{2+} luminescence spectra were excited by the 514.5 nm line of the Ar^+ ion laser and detected as describe above. NIR- Yb^{3+} downconversion was excited with a Ti: sapphire laser and detected using a liquid-nitrogen cooled Ge detector (ADC 403LS) and a Stanford Research SR830 lock-in amplifier. The laser beam was focused ($f=53 \text{ mm}$) on the crystal. All the spectra were corrected for the sensitivity of the monochromator and the detection system and for the refractive index of air (vacuum correction). They are represented as the number of photons per second versus wave numbers. For excitation spectra, the Ti: sapphire laser was scanned using an inchworm controlled (Burleigh PZ-501) birefringent filter and the wavelength was monitored with a wavemeter (Burleigh WA2100). For the two-color experiments, two Ti: sapphire lasers were used as excitation sources. Power-dependent excitation of the upconversion emission was measured using a neutral density filter wheel to attenuate the pump power. The laser power was measured with a power meter (Coherent Labmaster-E).

For time-resolved measurements, 10 ns pulses of the second harmonic of a Nd: YAG (Quanta Ray DCR 3) pumped dye laser (Lambda Physik FL3002; Pyridine 1 in methanol) was Raman shifted (Quanta Ray, RS-1, H_2 , 340 psi, operative range 935–1025 nm). The sample luminescence was dispersed by a 0.75 m single monochromator (Spex 1702) equipped with a 750 nm blazed 600 grooves/mm grating and detected using a multichannel scaler (Stanford Research SR430) for decay curves.

III. RESULTS

Figure 2 shows an overview of the unpolarized absorption spectra of RbMnCl_3 (right) and Yb^{3+} -doped RbMnCl_3 (left) at 11 K with Mn^{2+} and Yb^{3+} absorption peaks and their assignment. Polarized absorption measurements present an intensity difference between $\sigma(\mathbf{E}\perp\mathbf{c})$ and $\pi(\mathbf{E}\parallel\mathbf{c})$ spectra of the

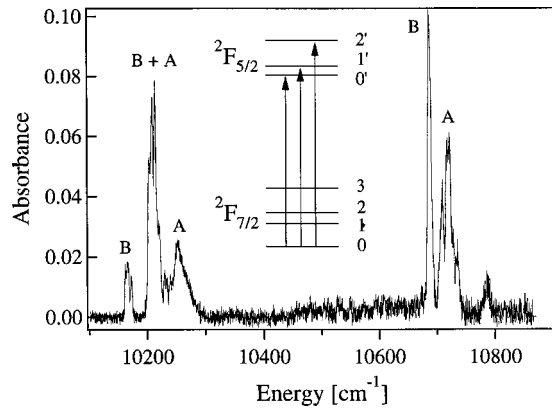


FIG. 3. Unpolarized optical absorption spectrum of $\text{RbMnCl}_3:0.08\% \text{Yb}^{3+}$ single crystal at 11 K. Sample thickness: 1.35 cm. The labels indicate absorption peaks corresponding to two different Yb^{3+} sites, A or B. The inset shows a schematic energy level and transition diagram of YbCl_6^{3-} .

less than 15% in the relevant spectral regions, therefore all the subsequent measurements were done unpolarized.

In Fig. 3 we show a high-resolution Yb^{3+} absorption spectrum at 11 K. Three transitions from the lowest Stark level of the ${}^2F_{7/2}$ ground state to the three levels of the ${}^2F_{5/2}$ excited state are expected for Yb^{3+} in trigonal symmetry, see inset in Fig. 3. However, twice this number of transitions is observed. We attribute this fact to the presence of two different Yb^{3+} sites in the RbMnCl_3 host lattice. The sharp peaks at 10 160, 10 205, and 10 686 cm^{-1} and 10 215, 10 247, and 10 710 cm^{-1} are assigned to sites B and A, respectively. Some of the bands show additional fine structure. The additional lines on the high-energy side of these peaks are assigned to vibronic features.

Fig. 4 shows high-resolution ${}^2F_{5/2} \rightarrow {}^2F_{7/2}$ luminescence spectra of $\text{RbMnCl}_3:\text{Yb}^{3+}$ at 10 K for two different excitation energies. The upper spectrum was excited at 10 686 cm^{-1} (site B) and the lower one at 10 715 cm^{-1} (site A). The $(0') \rightarrow (0,1,2,3)$ transitions (see inset) are found at 10 160, 10 025, 9860, and 9520 cm^{-1} and 10 215, 10 000, 9900, and 9640 cm^{-1} for sites B and A, respectively. These energies

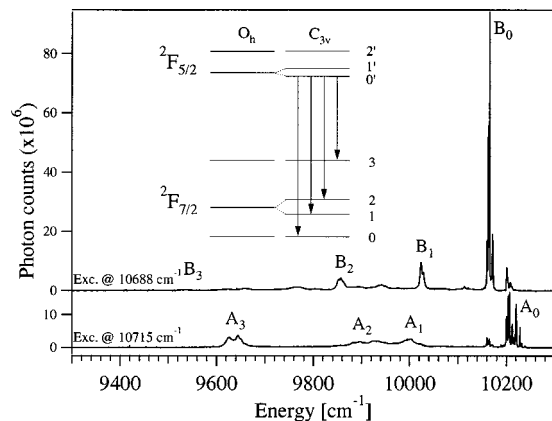


FIG. 4. 10 K unpolarized ${}^2F_{5/2} \rightarrow {}^2F_{7/2}$ luminescence spectra of $\text{RbMnCl}_3:\text{Yb}^{3+}$ excited site selectively at 10 686 cm^{-1} (top, site B) and 10 715 cm^{-1} (bottom, site A).

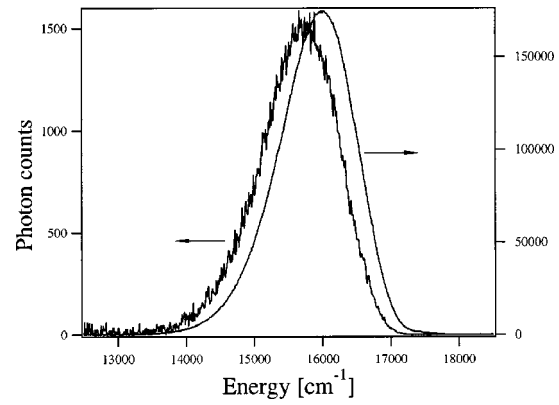


FIG. 5. Upconversion (thick line) and downconversion (thin line) luminescence spectra of $\text{RbMnCl}_3:\text{Yb}^{3+}$ under CW excitation at 10 686 and 19 436 cm^{-1} , respectively, at 10 K.

indicate a ground-state crystal-field splitting of 0, 135, 300, and 640 cm^{-1} (site B) and 0, 215, 315, and 575 cm^{-1} (site A). Both ground- and excited-state splittings show a trigonal component of the crystal field. This is shown in the energy-level diagram derived from the absorption and emission spectra for A and B sites (insets Figs. 3 and 4).

In $\text{RbMnCl}_3:\text{Yb}^{3+}$ excitation of Yb^{3+} around 10 700 cm^{-1} in the NIR at 10 K leads to orange $\text{Mn}^{2+} {}^4T_1 \rightarrow {}^6A_1$ upconversion luminescence as shown in Fig. 5. Also shown in Fig. 5 is the $\text{Mn}^{2+} {}^4T_1 \rightarrow {}^6A_1$ downconversion luminescence spectrum obtained after direct $\text{Mn}^{2+} {}^4T_1$ excitation at 19 436 cm^{-1} . Both bands have similar shapes, but the downconversion luminescence appears roughly 200 cm^{-1} higher in energy than the upconversion luminescence. The ratio of Yb^{3+} downconversion to Mn^{2+} upconversion luminescence intensity at 10 K after $\text{Yb}^{3+} {}^2F_{7/2} \rightarrow {}^2F_{5/2}$ excitation at 10 686 cm^{-1} (corrected for the detection system) was found to be approximately 50:1 for a typical excitation power of 200 mW (the beam being focused with a 53-mm focal lens). This value is four orders of magnitude higher than that observed in $\text{Cs}_3\text{Yb}_2\text{Br}_9$, comparing the green upconversion and NIR downconversion emission ratio originating from Yb^{3+} pairs ($2.1 \cdot 10^{-6}$).¹³

The 10 K NIR excitation spectrum of the VIS luminescence for $\text{RbMnCl}_3:\text{Yb}^{3+}$ is presented in Fig. 6. This upconversion excitation spectrum is similar to the absorption spectrum in Fig. 3; however, there are significant differences in the relative intensities of the peaks. Excitation peaks corresponding to site B are much more intense than those associated with site A. In the inset of Fig. 6, we plot the visible upconversion luminescence intensity versus the excitation power at 10 686 cm^{-1} on a double logarithmic scale. Within experimental accuracy, this system shows a quadratic power dependence below 50 mW indicating a two-photon excitation process. At excitation powers between 70 mW and 300 mW, the slope decreases to 1.7. In this experiment the Ti:sapphire excitation beam was focused to a diameter about 10 microns and, thus, we estimate that the x axis in the inset of Fig. 6 covers an excitation density range from 0 to roughly 380 W/cm^2 .

Figure 7 shows the normalized integrated intensity of the

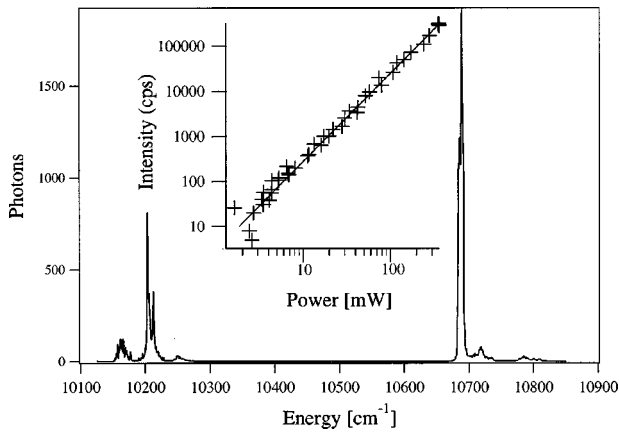


FIG. 6. 10 K excitation spectrum monitoring ${}^4T_1 \rightarrow {}^6A_1 \text{Mn}^{2+}$ upconversion luminescence at 15750 cm^{-1} . The spectrum is corrected for excitation laser power. The inset shows the upconversion luminescence intensity of $\text{RbMnCl}_3:\text{Yb}^{3+}$ at 15 K versus laser power obtained under 10686 cm^{-1} excitation in a double-logarithmic scale.

$\text{Mn}^{2+} {}^4T_1 \rightarrow {}^6A_1$ emission in $\text{RbMnCl}_3:\text{Yb}^{3+}$ after 19436 cm^{-1} downconversion excitation (\square) and after 10686 cm^{-1} upconversion excitation (\diamond) as a function of temperature. For comparison, the behavior of pure RbMnCl_3 after 19436 cm^{-1} excitation (\circ) is included. All three luminescences show qualitatively the same temperature dependence. The luminescence is quenched at higher temperatures. This quenching process is more efficient and sets in a lower temperature in the crystal containing ytterbium.

Figure 8 shows the time dependence of the 15 K Mn^{2+} upconversion luminescence intensity at 15750 cm^{-1} in $\text{RbMnCl}_3:\text{Yb}^{3+}$ after upconversion excitation at 10686 cm^{-1} with an excitation pulse of 10 ns width. The inset shows the same data in a semilogarithmic representation. The perfect single exponential decay ($\tau = 1.06 \text{ ms}$) and the absence of any rise are relevant for the identification of the upconversion mechanism, as will be discussed later. The same decay behavior was observed after excitation into the

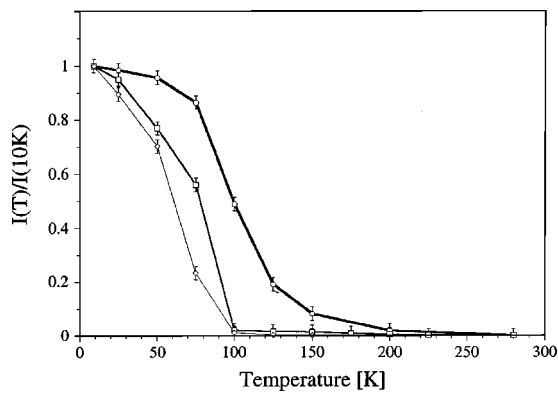


FIG. 7. Temperature dependence of the normalized integrated ${}^4T_1 \rightarrow {}^6A_1$ luminescence intensity of RbMnCl_3 and $\text{RbMnCl}_3:\text{Yb}^{3+}$ under green excitation at 19436 cm^{-1} , circles and squares, respectively, and exciting $\text{RbMnCl}_3:\text{Yb}^{3+}$ in the NIR at 10686 cm^{-1} (diamonds).

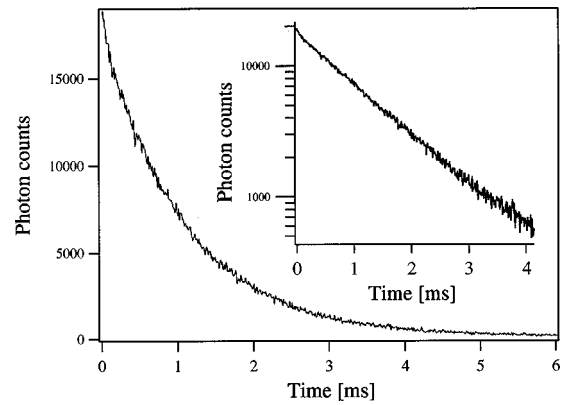


FIG. 8. Temporal behavior of the 15 K $\text{Mn}^{2+} {}^4T_1 \rightarrow {}^6A_1$ emission intensity after a short ($<10 \text{ ns}$) excitation pulse into the $\text{Yb}^{3+} {}^2F_{5/2}$ excited state at 10686 cm^{-1} (detecting 15750 cm^{-1}). The inset shows the same data in a semilogarithmic scale.

other Yb^{3+} absorption peaks. Direct excitation in the Mn^{2+} absorption band with short pulses gives rise to a similar behavior with a slightly longer lifetime for the ${}^4T_1 \text{Mn}^{2+}$ emission ($\tau = 1.10 \text{ ms}$).

Figure 9(b) presents the excited-state excitation (ESE) spectrum of $\text{RbMnCl}_3:\text{Yb}^{3+}$ at 15 K, shifted by 10215 cm^{-1} to higher energy, i.e., by the energy of the $\text{Yb}^{3+} {}^2F_{5/2}$ origin in order to make it comparable to the $\text{Mn}^{2+} {}^6A_1 \rightarrow {}^4E, {}^4A_1$ absorption spectrum that is shown in Fig. 9(b). In this experiment, a large $\text{Yb}^{3+} {}^2F_{5/2}$ population was provided by pumping into the $\text{Yb}^{3+} {}^2F_{7/2} \rightarrow {}^2F_{5/2}$ transition at 10715 cm^{-1} (typical excitation power 300 mW). The intensity of

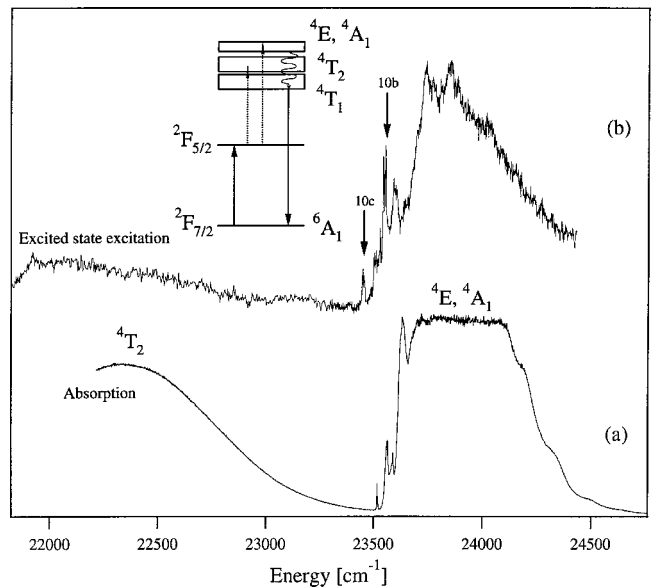


FIG. 9. (a) Unpolarized absorption spectrum of $\text{RbMnCl}_3:\text{Yb}^{3+}$ in the 4T_2 and ${}^4E, {}^4A_1$ region. (b) Two-color upconversion excitation spectrum (ESE) with a pump laser exciting at 10715 cm^{-1} and monitoring the $\text{Mn}^{2+} {}^4T_1$ emission while a laser probe is tuned in the $11500\text{--}14200 \text{ cm}^{-1}$ energy range. The ESE spectrum is shifted by $+10215 \text{ cm}^{-1}$ for comparison with (a) and corrected for the power of the probe laser. Both spectra were obtained at 15 K. The energy level scheme explains the principle of the experiment.

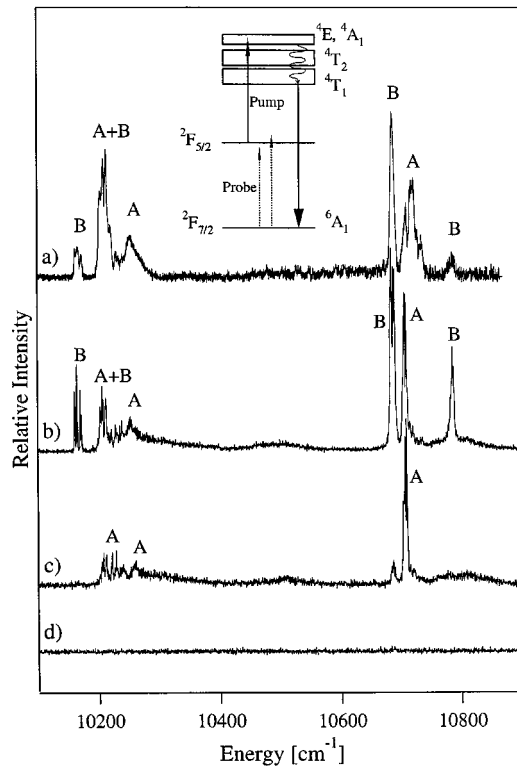


FIG. 10. Two color upconversion spectra at 15 K obtained by exciting with a pump laser at $13\,323\text{ cm}^{-1}$ (b) and $13\,218\text{ cm}^{-1}$ (c), and monitoring the $\text{Mn}^{2+} 4T_1 \rightarrow 6A_1$ emission while a laser probe is tuned through the $\text{Yb}^{3+} 2F_{7/2} \rightarrow 2F_{5/2}$ absorption peaks. The (d) signal corresponds to a wavelength scan without the pump laser. The principle of the experiment is explained in the inset. The 11 K absorption spectrum (a) with the site assignment is included for comparison.

the $\text{Mn}^{2+} 4T_1 \rightarrow 6A_1$ emission was then monitored as a function of the wavelength of a second probe laser (typical excitation power 50–80 mW). This excitation scheme is shown in the inset. The features observed in the ESE spectrum in the region of $4E, 4A_1$ origins are similar to the features observed in the Mn^{2+} ground-state absorption spectrum.

In a second two-color experiment (Fig. 10) a Ti-sapphire laser was used (typical excitation power 300 mW to pump at $13\,500\text{ cm}^{-1}$. At this energy there is neither Mn^{2+} nor Yb^{3+} ground-state absorption, but there is $2F_{5/2} (\text{Yb}^{3+}) \rightarrow 4E, 4A_1 (\text{Mn}^{2+})$ absorption. $\text{Mn}^{2+} 4T_1 \rightarrow 6A_1$ luminescence was monitored at $15\,750\text{ cm}^{-1}$ as a function of the wavelength of a second (probe) laser scanning through the $\text{Yb}^{3+} 2F_{7/2} \rightarrow 2F_{5/2}$ excitation region. The probe laser had a very low power (typically $\sim 200\text{ }\mu\text{W}$) to avoid one-color UC by the probe beam alone, while scanning through the Yb^{3+} absorption peaks [Fig. 10(d)]. The spectra obtained from these experiments are shown in Figs. 10(b) and 10(c). They were excited at the positions marked 10(b) and 10(c) in Fig. 9, respectively. Figures 10(b) and 10(c) correspond to the $2F_{7/2} \rightarrow 2F_{5/2}$ absorption spectrum of Yb^{3+} , which is shown for comparison in Fig. 10(a). Depending on the excitation energy of the pump laser, Yb^{3+} ions in different sites are involved in the upconversion process, thus the difference be-

tween Figs. 10(b) and 10(c). The excitation scheme of this experiment is shown in the inset.

IV. DISCUSSION

A. Crystal structure and charge compensation

In order to understand this unusual upconversion phenomenon, it is important to examine the crystal structure of the title compound. RbMnCl_3 crystallizes in the space group $P6_3/mmc$ ¹⁴ with lattice parameters $a=7.16\text{ }\text{\AA}$ and $c=17.83\text{ }\text{\AA}$, $Z=6$, at room temperature. The structure type can be described as intermediate between the CsNiCl_3 structure, which consists of infinite linear chains of face-sharing octahedra, and the KNiF_3 perovskite structure, which consists of a three-dimensional network of corner-sharing octahedra. As illustrated in Fig. 11(a), the compound consists of face-sharing octahedral dimers (site B) along the c axis linked three dimensionally by corner-sharing octahedra (site A); i.e., two octahedra containing Mn^B ions share a face forming a $\text{Mn}_2\text{Cl}_6^{5-}$ unit that then shares corners with six different octahedra containing Mn^A manganese ions. The Mn^A ion occupies a site having D_{3d} symmetry, while Mn^B is in C_{3v} site symmetry.

It is well established that salts such as CsMgCl_3 and CsCdBr_3 , which adopt the linear chain CsNiCl_3 structure, have a pronounced tendency to incorporate trivalent ion impurities into the lattice as discrete and well-defined pairs.¹⁵ This tendency of trivalent impurities to cluster in pairs arises from the charge compensation requirements of the linear-chain lattice when the trivalent rare earth substitutes for the divalent cations. Three neighboring divalent ions are replaced by two rare earth (RE^{3+}) ions with a divalent vacancy in the middle. Unlike compounds with a one-dimensional chain structure, this type of charge compensation is not possible in RbMnCl_3 . This lattice shows more possibilities for charge compensation as a consequence of the two distinct Mn^{2+} sites.

Both sites A and B are available for Yb^{3+} . Two different Yb^{3+} sites have been found in the absorption (Fig. 3) and emission spectra (Fig. 4). It is therefore tempting to assign them to the two sites A and B, respectively. It is also possible, however, that only one of the crystallographic sites can accommodate Yb^{3+} , and the two Yb^{3+} sites found spectroscopically correspond to different charge compensation arrangements. The D_{3d} Mn^{2+} site (Mn^A) is smaller than the C_{3v} Mn^{2+} site (Mn^B): mean Mn-Cl distances of 2.48 and 2.55 \AA , respectively. The Yb^{3+} ionic radius is slightly bigger than the Mn^{2+} ionic radius, 0.87 and 0.83 \AA ,¹⁶ respectively. Therefore, it is more likely that Yb^{3+} substitutes for the Mn^B site and that there is a charge-compensating vacancy at the Mn^A site. Four different possibilities for Yb^{3+} pair arrangements and charge compensations with at least one Yb^{3+} on a Mn^B site are displayed in Fig. 11(b).

B. Yb^{3+} sites and energy levels

The Stark splittings of the $2F_{7/2}$ and $2F_{5/2}$ multiplets are very sensitive to low-symmetry distortions of the octahedral environment. In trigonal symmetry (C_{3v}) the $2F_{7/2}$ ground

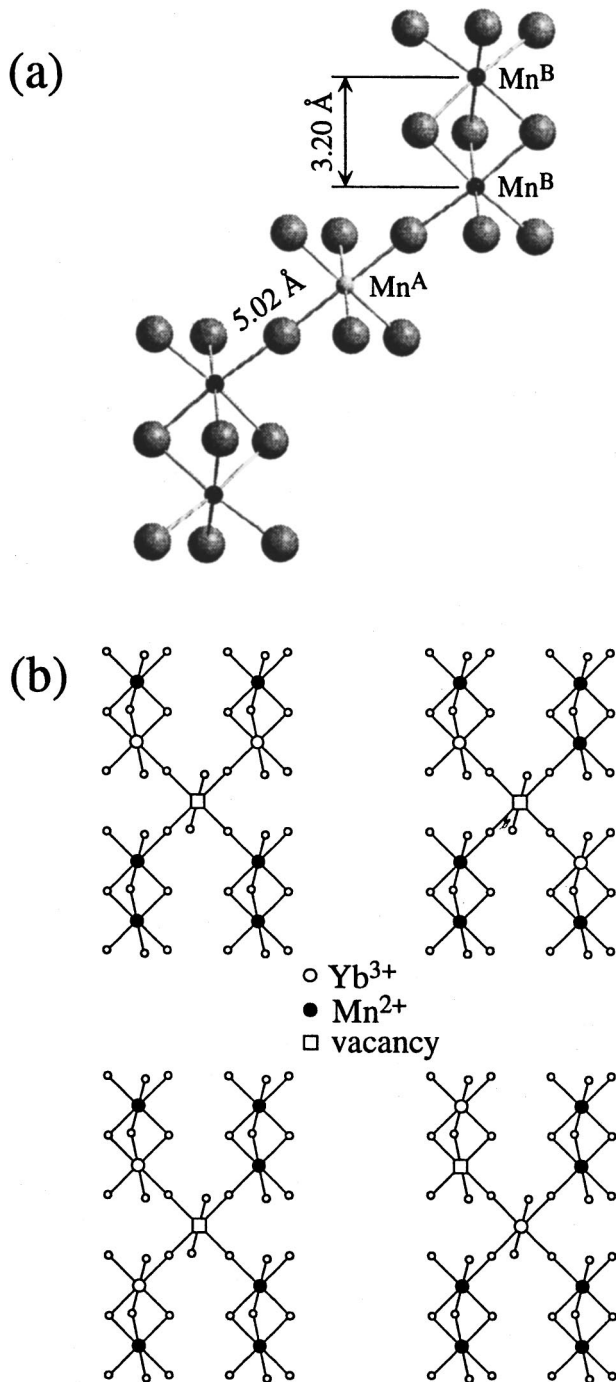


FIG. 11. (a) Relevant elements of the RbMnCl₃ crystal structure illustrating the two types of Mn sites, $D_{3d}(\text{Mn}^A)$ and $C_{3v}(\text{Mn}^B)$ and bridging geometries (face and corner sharing octahedra). (b) Possible arrangements of Yb³⁺ ions in pairs with charge compensation vacancies. The chloride ions occupy the corners of the octahedra.

state and the ${}^2F_{5/2}$ excited state are split in four and three Stark levels labeled as 0, 1, 2, 3, and 0', 1', 2', respectively. The possible charge compensations shown in Fig. 11(b) will lead to small nonaxial crystal field components in each case. This will not lead to any additional splittings but slightly affect the relative energies of the Yb³⁺ Stark levels. The 11

TABLE I. Energies of the crystal field levels of Yb³⁺ doped RbMnCl₃ derived from high-resolution absorption and emission spectra at 10 K. Energies are given in cm⁻¹ relative to the lowest-energy Stark level. A and B correspond to two inequivalent Yb³⁺ sites.

Crystal Field Level		A	B
${}^2F_{7/2}$	(0)	0	0
	(1)	215	135
	(2)	315	300
	(3)	575	640
${}^2F_{5/2}$	(0')	10 215	10 160
	(1')	10 247	10 205
	(2')	10 710	10 686

K unpolarized absorption spectrum (Fig. 3) is roughly a superposition of two spectra corresponding to Yb³⁺ in two inequivalent crystallographic sites with approximate trigonal symmetry. The absence of strong vibronic bands in the absorption and emission spectra in the ${}^2F_{7/2} \leftrightarrow {}^2F_{5/2}$ region shows that the Yb³⁺ ions are located in noncentrosymmetric sites with a large odd-parity crystal-field component.

In Fig. 4, 10 686 and 10 715 cm⁻¹ excitations give rise to completely different emission spectra in the ${}^2F_{5/2} \rightarrow {}^2F_{7/2}$ region. Based on the temperature dependence, cold and hot bands were identified. According to emission and absorption, the crystal field splittings of the ground state and excited state for sites A and B collected in Table I were derived. In deriving these numbers, the fine structure of the bands observed in Figs. 3 and 4, which has a magnetic origin as will be discussed below, was not taken into account, i.e., the barycenters of the split bands were used. Ground- and excited-state splittings are quite similar to those found in Cs₃Lu₂Cl₉:Yb³⁺.¹⁷ Additional bands are observed in emission due to some thermal population of (1') at 10 K. The origins of the Yb³⁺ ${}^2F_{5/2} \rightarrow {}^2F_{7/2}$ emissions due to sites A and B are 40 cm⁻¹ apart, with the B line lower in energy. In the temperature range 10–100 K selective A and B excitation leads to almost exclusive A and B emission, respectively, i.e., there is no evidence for substantial intersite energy transfer in this temperature range. The extra fine structure observed in some of the absorption and emission bands is ascribed to the fact that the host lattice RbMnCl₃ is magnetically ordered below $T_N \sim 94$ K.¹⁸ Since the exchange coupling between neighboring Mn²⁺ ions is expected to be stronger than the Yb³⁺-Mn²⁺ coupling, the Yb³⁺ ions are exposed to a molecular field, i.e., an internal magnetic field created by the ordered magnetic moments of the Mn²⁺ ions leading to a Zeeman splitting of the Yb³⁺ levels.

C. Mn²⁺ spectroscopy and excited-state dynamics

The absorption spectrum of RbMnCl₃ in Fig. 2 in the visible and near ultraviolet (UV) is readily assigned to d - d excitations as indicated. For a $3d^5$ electron configuration with a 6A_1 ground state, all these transitions are both spin and parity forbidden in octahedral coordination. This spec-

trum is a good illustration of the environmental effects on the $3d$ electrons of Mn^{2+} . In contrast to f - f spectra of lanthanides, which consist of sharp lines, some of the absorption bands of RbMnCl_3 are broad, corresponding to $t_2 \rightarrow e$ electron promotions, and others are sharp, corresponding to spin-flip transitions within the $(t_2)^3(e)^2$ ground electron configuration. The ${}^2F_{7/2} \rightarrow {}^2F_{5/2}$ absorption band of Yb^{3+} doped in RbMnCl_3 around $10\,000\text{ cm}^{-1}$, which is also shown in Fig. 2, has the typical line shape of f - f transitions.

The broad emission band shown in Fig. 5 is due to the ${}^4T_1 \rightarrow {}^6A_1$ transition of Mn^{2+} in a slightly distorted octahedral coordination of chloride ions. Its maximum is Stokes shifted at 12 K by about 3000 cm^{-1} from the corresponding ${}^6A_1 \rightarrow {}^4T_1$ absorption maximum due to the excited-state distortion. Its width is due to a contraction of the MnCl_6^{4-} octahedron in the 4T_1 state with respect to the 6A_1 ground state. The latter derives from a $(t_2)^3(e)^2$ electron configuration, whereas the former results from $(t_2)^4(e)^1$ in the strong-field limit. This distortion of the emitting state of Mn^{2+} is relevant for the discussion of the UC properties. In Fig. 5 we observe an energy redshift of about 200 cm^{-1} at 10 K of the emission band excited by upconversion compared to the emission band obtained by direct green excitation. This redshift of the UC excited emission is significant. It immediately tells us that the emissions excited in the green and in the NIR originate from different subsets of Mn^{2+} ions in the crystal at 10 K. As will be shown below the dopant Yb^{3+} ions are involved in the NIR excitation process. The neighboring Mn^{2+} ions are perturbed by the presence of Yb^{3+} and will exhibit a slightly different crystal field. Since Yb^{3+} ions are larger (ionic radius 0.87 \AA) than Mn^{2+} ions (ionic radius 0.83 \AA),¹⁶ this likely leads to a squeezing of the Mn^{2+} coordination in the neighborhood of Yb^{3+} . This, in turn, leads to a slight increase of the crystal field resulting in the observed redshift. This explanation implies that the Mn^{2+} excitation remains essentially trapped at 10 K. This has been shown to be true in previous spectroscopic work on RbMnCl_3 . The self-trapping of the Mn^{2+} excitation at low temperatures is essentially due to the geometrical distortion of the 4T_1 excited state, which needs to be thermally activated for extensive energy migration.¹⁹

Figure 7 shows that irrespective of the excitation mode, the Mn^{2+} luminescence of $\text{RbMnCl}_3:\text{Yb}^{3+}$ is thermally quenched on increasing the temperature to 100 K. A similar quenching is also observed in pure RbMnCl_3 , included in Fig. 7 for comparison, but it occurs at a somewhat higher temperature. This quenching is common to all undiluted Mn^{2+} chloride compounds with the exception of $[(\text{CH}_3)_4\text{N}]\text{MnCl}_3$ (TMMC), and it has been ascribed to thermally activated energy migration to killer traps. In TMMC, the energy migration is restricted to one dimension and thus less efficient. The most likely traps are impurity ions such as Cu^{2+} , Fe^{2+} , or Mn^{3+} . The latter is a prime candidate, and it has been shown that reducing the Mn^{3+} impurity concentration in RbMnCl_3 increases the quenching temperature. This was achieved by adding Mn metal to the melt in the Bridgman growth of RbMnCl_3 .²⁰ For the synthesis of our Yb^{3+} -doped RbMnCl_3 crystals, the situation is more compli-

cated. Addition of Mn metal to the melt was found to lead to an absorption band at $25\,000\text{ cm}^{-1}$, a strong indication for the presence of Yb^{2+} ions in the crystal. It appears that the redox potentials of the $\text{Mn}^{2+}/\text{Mn}^{3+}$ and $\text{Yb}^{2+}/\text{Yb}^{3+}$ couples under melting conditions are such that ytterbium is preferentially reduced and we are left with some Mn^{3+} impurities. We ascribe the fact that the Mn^{2+} emission is quenched at lower T in the doped crystal to the higher concentration of Mn^{3+} . The faster thermal quenching of the Mn^{2+} emission in the Yb^{3+} -doped RbMnCl_3 is due to an additional depopulation channel, intrinsic to the Yb^{3+} -doped samples, from the Mn^{2+} emitting state to the ${}^2F_{5/2}$ Yb^{3+} level. This quenching process is already present at low temperatures, it becomes evident as $\text{Yb}^{3+} {}^2F_{5/2} \rightarrow {}^2F_{7/2}$ emission after direct Mn^{2+} excitation at 514.5 nm .

D. Upconversion

1. General considerations

The observation of visible Mn^{2+} emission after NIR Yb^{3+} excitation is remarkable in itself. Upconversion phenomena are rather common in lanthanide-doped crystals and glasses. This is due to the presence of more than one metastable f - f excited state that, in turn, is the result of weak electron-phonon coupling. In transition metal ion-doped crystals and glasses, on the other hand, multiphonon relaxation processes are much more competitive. As a result, multiple excited-state emission and upconversion phenomena are very rare. We have recently started a systematic study of such effects and we have identified a number of systems in which UC can occur: Ti^{2+} , Ni^{2+} , Mo^{3+} , Re^{4+} , and Os^{4+} (Refs. 2–6) in various halide lattices. A significant difference between transition metal and rare earth metal ion-doped upconversion systems lies in the fact that the d electrons are less shielded and thus more susceptible to changes in their environment. We have found that this provides an opportunity to tune the UC properties by chemical and structural variation.⁴ Another important difference is that spin is a good quantum number in $3d$ and $4d$ transition metals.^{2,4} As a consequence, we can influence the UC behavior by magnetic perturbations.²¹

The combination of transition-metal and lanthanide-metal ions in the same crystal increases our possibilities of creating and varying upconversion processes by chemical variation. Our title system, Yb^{3+} -doped RbMnCl_3 , provides a nice example for observing a completely new phenomenon. The involvement of Mn^{2+} in an upconversion process is unexpected, and with the exception of our recent brief paper, has not been described in the literature.

The NIR excitation spectrum of the upconverted visible luminescence in Fig. 6 directly proves the involvement of Yb^{3+} in the UC process. The excitation spectrum follows the absorption spectrum, and we notice that the site B excitations are more efficient than the site A excitations in inducing upconversion by about a factor of 100 at 10 K. The dependence of the Mn^{2+} luminescence intensity on the power of the Yb^{3+} laser excitation at $10\,686\text{ cm}^{-1}$ clearly identifies the excitation as a two-photon process.²² This is documented by the slope of two in the double-logarithmic power plot in the inset of Fig. 6.

Having established the ${}^2F_{5/2}$ excited state around $10\,000\text{ cm}^{-1}$ as the intermediate state and the 4T_1 state of Mn^{2+} around $17\,400\text{ cm}^{-1}$ (energy of origin) as the emitting state we proceed to a discussion of possible mechanisms.

The schemes in Figs. 1(a) and 1(b) represent the most common UC processes encountered in lanthanide systems. A sequence of ground and excited state absorption (GSA and ESA) steps on a single ion can lead to UC [Fig. 1(a)]. This mechanism has two characteristic features: (i) It contains the signatures of both GSA and ESA steps in its excitation spectrum, and (ii) In an experiment with pulsed excitation, both steps must occur within the excitation pulse, and a pure decay of the upconverted luminescence will be observed. In $\text{RbMnCl}_3:\text{Yb}^{3+}$ we can rule out a GSA/ESA sequence on a single ion, because both Yb^{3+} and Mn^{2+} are involved. Nevertheless, the two characteristic features (i) and (ii) will be relevant in our case.

The second important UC process, represented in Fig. 1(b), involves excitations to the intermediate level on two neighboring centers and a subsequent energy-transfer step. This mechanism only carries the GSA fingerprint in its excitation spectrum, and the characteristic feature is a rise of the upconverted luminescence after the excitation is deposited in the intermediate level by a laser pulse. This GSA/ETU mechanism is very common in lanthanide systems. In $\text{RbMnCl}_3:\text{Yb}^{3+}$ it can be ruled out because Mn^{2+} has no intermediate level around $10\,000\text{ cm}^{-1}$.

The schemes in Figs. 1(c), 1(d), and 1(e) represent some alternative UC excitation schemes that may be relevant in $\text{RbMnCl}_3:\text{Yb}^{3+}$. The mechanisms 1(c) and 1(d) have been discussed in the literature for explaining the observation of visible Tb^{3+} emission in $\text{Tb}^{3+}/\text{Yb}^{3+}$ -codoped CaF_2 , SrF_2 (Ref. 23) and YF_3 (Ref. 24) after NIR Yb^{3+} excitation. The process 1(c) is a three-ion process and relies on the presence of two close-by excited Yb^{3+} ions that can jointly transfer their excitation to Tb^{3+} . The process 1(d) is a higher-order process based on multipole-multipole energy transfer occurring simultaneously with a GSA on the acceptor. The process [Fig. 1(c)] is expected to show a rise time, and we thus rule it out. The process [Fig. 1(d)] has never been confirmed in an experimental situation, and we rule it out on the basis of its expected low efficiency.

2. Time and wavelength dependence of the upconversion process

By measuring the time evolution of the upconverted luminescence intensity after a short excitation pulse, we can learn a great deal about the mechanism, because different rise and decay characteristics are expected for the various mechanisms in Fig. 1. The experimental data for $\text{RbMnCl}_3:\text{Yb}^{3+}$ at 15 K are presented in Fig. 8. In this experiment, the laser pulse has a duration of about 10 ns, and the luminescence intensity was registered between 500 ns and 6 ms after the pulse. In this time range, we find a pure single-exponential decay corresponding to a lifetime τ of 1.06 ms, and we do not find any evidence of a rise. This immediately rules out an energy-transfer step, which is slower than 500 ns. Upconversion processes occurring by a GSA/ETU mechanism in lanthanide-doped crystals usually have rise times on the order of milliseconds, and we can

expect similar rate constants for the energy-transfer processes involved in processes 1(c) and 1(d) of Fig. 1. The nonobservation of a rise thus rules out these mechanisms. Our decay data clearly indicate a GSA/ESA-type mechanism, with both steps happening within the duration of the laser pulse. The lifetime of 1.06 ms at 15 K derived for the upconverted Mn^{2+} luminescence is similar to the Mn^{2+} lifetime of 1.10 ms obtained by direct Mn^{2+} excitation in the green at the same temperature. The slight but significant difference between the two reflects the fact that different subsets of Mn^{2+} ions are involved in the two experiments. As discussed in Sec. IV C, the Mn^{2+} ions involved in the UC process are located in the neighborhood of the Yb^{3+} ion. Green excitation, on the other hand excites the ‘‘bulk’’ Mn^{2+} ions in a slightly different coordination, and thus the shift in Fig. 5.

Further evidence for a GSA/ESA sequence is provided by the dependence of the UC luminescence intensity on the excitation wavelength. A GSA/ESA sequence must show up in the excitation spectrum, with both steps leaving their trace. Let us first discuss our one-color UC experiment with the excitation spectrum in Fig. 6. This corresponds very well to the absorption spectrum, proving the GSA step. But there are no features pointing to the ESA step. This is explained by referring to Fig. 2. The $10\,686\text{ cm}^{-1}$ ESA step hits the Mn^{2+} between the broad 4T_1 and 4T_2 absorption maxima in a spectral region with very small and essentially wavelength independent absorption cross section. This explains the absence of any ESA fingerprint in the one-color UC experiment. It also explains the relative inefficiency of the UC process. For $10\,686\text{ cm}^{-1}$ excitation of 200 mW (the beam being focused with a lens of 53-mm focal length), we find that four percent of the Yb^{3+} excitation is upconverted at 10 K leading to an efficiency (VIS photons vs NIR photons) of two percent. Under the same conditions, we obtain significantly higher UC efficiencies in $\text{CsMnCl}_3:\text{Yb}^{3+}$,¹¹ and we ascribe at least part of this difference to the inefficiency of the ESA step in the title compound.

Two-color excitation experiments provide conclusive proof for a GSA/ESA sequence. We have done experiments pumping both the GSA and ESA steps with intense laser beams and probing the ESA and GSA steps, respectively, by scanning with a lower-intensity beam over the relevant spectral regions. The results are shown in Figs. 9 and 10, and will now be discussed in detail. The relevant excitation and relaxation schemes are included as insets in these figures.

In the first experiment (Fig. 9) the pump beam (350 mW) was fixed at $10\,686\text{ cm}^{-1}$, the strongest Yb^{3+} absorption at 15 K, see Fig. 3. The probe beam (50 mW) was scanned over the region of 4T_2 and 4A_1 , 4E excited-state absorptions. An increase of the upconverted Mn^{2+} emission of up to 40% was observed upon addition of the probe beam. Since the pump beam is much more intense in this experiment, there is relatively intense underlying one-color UC from the pump beam alone. Spectrally, this excited-state excitation spectrum ESE, after shifting it to higher energy by $10\,215\text{ cm}^{-1}$, the energy of the lowest ${}^2F_{5/2}$ Stark level of Yb^{3+} , is in nice agreement with the GSA spectrum of RbMnCl_3 in the region of 4T_2 and 4A_1 , 4E bands, see Fig. 9. In particular, there are

sharp features in the origin region of the 4A_1 , 4E excitations in both spectra. This provides strong support that the second laser beam actually probes the ESA step. We notice that there is not an exact coincidence of the sharp origin lines in the two spectra. The first lines in the ESE spectrum lie below the first line in absorption. These differences are ascribed to the fact that the two experiments are again probing different subsets of Mn^{2+} ions. The absorption spectrum is the bulk spectrum, whereas the ESE spectrum probes the Mn^{2+} ions in the neighborhood of Yb^{3+} , which are involved in upconversion. In the case of 4T_1 excitations there is an energy shift of 200 cm^{-1} between the two sets, see Sec. IV C and Fig. 5. In the case of 4A_1 , 4E excitations the differences are smaller, because these excited states are crystal-field independent in first order. The Mn^{2+} ions involved in the UC process are in a slightly squeezed octahedral situation leading to a slight reduction of the Racah parameters of about 0.2%.

In the second two-color experiment (Fig. 10) the role of the two beams was reversed in order to eliminate one-color upconversion. The pump beam (300-mW power) was fixed to the ESA peaks indicated by the two arrows in Fig. 9, corresponding to $13\,323\text{ cm}^{-1}$ Fig. 10(b) and $13\,218\text{ cm}^{-1}$ Fig. 10(c), respectively. At these wavelengths, the crystal is completely transparent, i.e., there is no ground-state absorption and, consequently, no upconversion. Addition of a very weak (200 μW) probe beam scanning the ${}^2F_{7/2} \rightarrow {}^2F_{5/2}$ GSA region of Yb^{3+} then leads to upconversion, and the excitation spectra for the two pump wavelengths are shown in Figs. 10(b) and 10(c). Figure 10(a) shows an absorption spectrum at the same temperature for comparison, and Fig. 10(d) is a trace obtained in the absence of the pump beam. No UC luminescence is detectable under the conditions of Fig. 10(d), i.e., with a very weak laser beam incapable of inducing one-color UC. The ESA pump beam is essential, and it leads to very intense UC luminescence despite the weakness of the GSA excitation beam. This is the final and perhaps most definitive proof of the importance of the ESA step in the upconversion mechanism. We can even site resolve the upconversion process as demonstrated by the difference of Figs. 10(b) and 10(c). The two pump laser lines at $13\,323\text{ cm}^{-1}$ [Fig. 10(b)] and $13\,218\text{ cm}^{-1}$ [Fig. 10(c)] coinciding with different sharp features in the 4A_1 , 4E excitation region, see arrows in Fig. 9, correspond to ESA transitions in different sites. Consequently, Fig. 10(c) is a pure site *A* excitation spectrum and Fig. 10(b) a dominant site *B* spectrum.

3. Upconversion based on exchange interactions

A sequence of GSA/ESA for the upconversion process in $\text{RbMnCl}_3:\text{Yb}^{3+}$ is established beyond doubt. We thus have important fingerprints of the mechanism in Fig. 1(a). However, this is a single-ion mechanism, and in our case, it is clear that two ions are involved. The intermediate state is the ${}^2F_{5/2}$ excited state of Yb^{3+} and the emitting state is the 4T_1 state of Mn^{2+} . We thus have to look beyond the established upconversion mechanisms in Figs. 1(a)–Figs. 1(d) to explain our phenomenon.

In the literature we find a good basis for a plausible UC mechanism in $\text{RbMnCl}_3:\text{Yb}^{3+}$. In Cr^{3+} -doped EuAlO_3 crys-

tals it was found that besides the normal ${}^2E \rightarrow {}^4A_2$ *R* line emission of Cr^{3+} there were emission lines further in the IR. These lines, which are completely absent in Cr^{3+} -doped Al_2O_3 are intense, some of them more intense than the *R* lines. Their energy shift from the *R* lines was found to correspond to energy differences between the 7F_0 ground multiplet of Eu^{3+} and the 7F_J ($J=1-6$) excited multiplets. These transitions can therefore be viewed as two-ion processes in which a ${}^2E \rightarrow {}^4A_2$ de-excitation on Cr^{3+} occurs simultaneously with a ${}^7F_0 \rightarrow {}^7F_J$ excitation, leading to a radiative process at the energy difference. The authors of Refs. 25 and 26 convincingly argued that exchange interactions between the magnetic ions Cr^{3+} and Eu^{3+} were likely responsible for this observation. A mechanism based on a multipole-multipole energy-transfer process coupled to a radiative transition [process Fig. 1(d)] could be ruled out on the basis of the high efficiency.

Our Yb^{3+} -doped RbMnCl_3 system is in a significant way similar to Cr^{3+} -doped EuAlO_3 . We therefore believe that a similar mechanism is operative, for the first time leading to a photon upconversion. Despite the fact that we cannot unambiguously identify the Yb^{3+} sites in RbMnCl_3 (see below), we can be certain that the Yb^{3+} ions substitute for Mn^{2+} ions and thus have intimate contact, either through corner or face sharing octahedra, with the neighboring Mn^{2+} ions. These contacts provide the pathways for Yb^{3+} - Mn^{2+} exchange interactions. And we can expect these interactions to be on the same order of magnitude as in $\text{EuAlO}_3:\text{Cr}^{3+}$, because in both systems a $4f$ ion couples to the $3d$ ion.

The simplest picture to view the situation in $\text{RbMnCl}_3:\text{Yb}^{3+}$ is that of an exchange-coupled Yb^{3+} - Mn^{2+} dimer. This is a gross simplification, because a given Yb^{3+} ion is likely to have more than one Mn^{2+} nearest neighbors in this lattice (see below), but it is sufficient to explain all of the main features of the upconversion process. Taking an Yb^{3+} - Mn^{2+} dimer as the relevant chromophoric unit for our observations, we obtain a simple and straightforward situation depicted in Fig. 12. The dimer ground state is $|{}^2F_{7/2} {}^6A_1\rangle$. The intermediate dimer state is $|{}^2F_{5/2} {}^6A_1\rangle$. As a result of the exchange coupling this state is dominantly, but not fully, localized on Yb^{3+} . Similarly, the $|{}^2F_{7/2} {}^4T_1\rangle$ and $|{}^2F_{7/2} {}^4T_2\rangle$ higher-excited states are mainly, but not fully, localized on the Mn^{2+} . In other words, with the dimer as the relevant optical unit, we have a GSA/ESA upconversion mechanism as depicted in Fig. 1(a). In order to emphasize the fact that two ions are involved, we have drawn the pictogram in Fig. 1(e) to account for the present situation.

More than 30 years ago, Tanabe formulated the mechanism by which transitions in exchange-coupled dimers of transition metal ions can gain intensity.¹⁰ A pair of ions can interact with the electric vector (**E**) of the radiation field. The essential feature of the Tanabe mechanism is that the transition dipole moment **P** is spin dependent. For our Yb^{3+} - Mn^{2+} pair we might formulate it as follows,

$$\mathbf{P} = \sum_{i=1}^5 \mathbf{\Pi}_{\text{Yb Mn}_i} (\mathbf{S}_{\text{Yb}} \cdot \mathbf{s}_{\text{Mn}_i}), \quad (1)$$

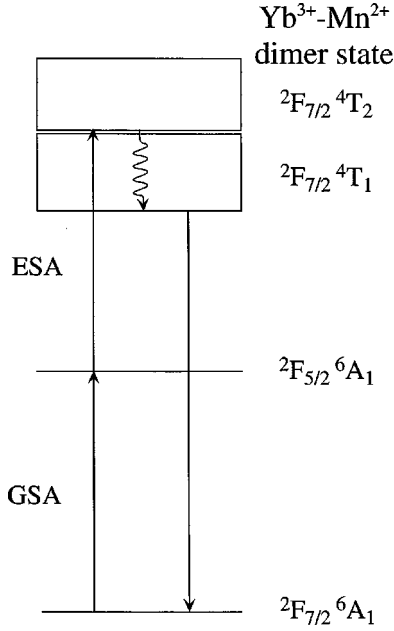


FIG. 12. Representation of the upconversion process in $\text{RbMnCl}_3:\text{Yb}^{3+}$ in a dimer picture. Full arrows indicate radiative processes of GSA, ESA, and luminescence, and the wavy arrow corresponds to a multiphonon relaxation process. The states are labeled in a $\text{Yb}^{3+}\text{-Mn}^{2+}$ dimer notation.

where i refers to the five d orbitals on Mn^{2+} . The components $\Pi_{\text{Yb Mn}_i}$ of the Π vectors are related to the corresponding orbital exchange parameters $J_{\text{Yb Mn}_i}$ as follows,

$$\Pi_{\text{Yb Mn}_i} = \left(\frac{\partial J_{\text{Yb Mn}_i}}{\partial E} \right)_{E \rightarrow 0}, \quad (2)$$

where E is the respective component of the radiation field. This means that the Tanabe mechanism is efficient wherever there are efficient exchange pathways. We do not know the size of the exchange parameters governing the $\text{Yb}^{3+}\text{-Mn}^{2+}$ coupling, but we can make some reasonable guesses. Within the series of face-sharing dimers, $\text{Yb}_2\text{Br}_9^{3-}$, YbCrBr_9^{3-} , and $\text{Cr}_2\text{Br}_9^{3-}$, the size of the exchange coupling was determined by inelastic neutron scattering. Total ground-state splittings of 2.9, 9.6, and 48 cm^{-1} were determined for the three complexes, respectively.²⁷ We take this as an indication of how exchange interactions grow in corresponding f - f , f - d , and d - d dimers. Another estimation of the $\text{Yb}^{3+}\text{-Mn}^{2+}$ coupling strength in the present system is provided by the observed fine structure in the Yb^{3+} absorption and emission lines, which we ascribe to exchange interactions. Taking as an example, the band B_0 in Fig. 4, we measure a total spread of 12 cm^{-1} between the highest and the lowest line. On the basis of these considerations, the observation of oscillator strength induced by a Tanabe mechanism in a $\text{Yb}^{3+}\text{-Mn}^{2+}$ dimer becomes plausible.

This mechanism has been found to explain spectral features such as magnon sidebands in magnetically ordered transition-metal insulators. But it has also been used to interpret the optical spectra of numerous dimers and a higher

cluster of exchange-coupled $3d$ ions. It leads to an enhancement of the intensity of nominally forbidden transitions. This enhancement can be orders of magnitude in transition-metal ion systems. The spin and parity forbidden ${}^3T_{1g} \rightarrow {}^1E_g({}^1T_{2g})$ absorption in Ti^{2+} -doped MnCl_2 , for instance, is at least three orders of magnitude more intense than in Ti^{2+} -doped MgCl_2 .² Transitions to doubly excited states in magnetically coupled Cr^{3+} and Mn^{2+} systems are prominent examples of excitations that cannot occur on a single ion and that are therefore enabled by the Tanabe mechanism. In our present situation, the Tanabe mechanism is somewhat less efficient than in pure transition metal ion systems, but on the basis of the above number we can still expect a sizable effect. With reference to Fig. 12, we expect a slight enhancement of the GSA step. Much more important is the ESA step, which is enabled by this mechanism. It involves electronic changes on both partners of the dimer, quite analogous to a double excitation in a Cr^{3+} dimer.

Let us finally return to Fig. 11 and the various possible Yb^{3+} sites. On the basis of our present knowledge, we cannot unambiguously correlate the Yb^{3+} sites A and B with the pictures in Fig. 11(b). From the absorption spectrum we know that the two major Yb^{3+} sites A and B occur in about the same concentration. And from the UC excitation spectrum, we know that site B is more efficient than site A by a factor of 100 in inducing upconversion. We ascribe this distinct behavior to a difference in the $\text{Yb}^{3+}\text{-Mn}^{2+}$ bridging geometry. One is likely a corner-sharing chloride bridge and the other one a face-sharing chloride bridge. We are in the process of systematically studying other Yb^{3+} -doped halides lattices with well-defined bridging geometries to shed more light on this question.

V. CONCLUSION

We have identified and characterized an upconversion phenomenon in Yb^{3+} -doped RbMnCl_3 . Excitation of Yb^{3+} around $1 \mu\text{m}$ leads to orange Mn^{2+} luminescence at low temperatures. We propose a mechanism based on exchange interactions between the Yb^{3+} and Mn^{2+} ions to account for this phenomenon.

The combination of transition-metal and rare-earth-metal ions in the same crystal evidently opens pathways and mechanisms for NIR to VIS upconversion processes. We are presently engaged in a systematic study of such systems and processes. Our main objective is a fundamental understanding of the underlying mechanisms. Such understanding is an important prerequisite for designing new light emitting materials and processes. Transition metal ion systems are much more susceptible to small chemical and structural variations than lanthanide systems. As an example, we mention some preliminary results on Yb^{3+} -doped CsMnCl_3 , which are in some respects, significantly different from those reported here. On the one hand, this susceptibility requires very detailed studies to understand its origin. On the other hand, it provides a handle to tune the light emission properties once the basic mechanisms are understood.

ACKNOWLEDGMENTS

The authors are grateful to Markus Wermuth and Daniel Gamelin for fascinating discussions on upconversion phe-

nomena and their constant interest in this work. The financial support of the Swiss National Science Foundation is acknowledged.

-
- *Corresponding author. Fax: +41 031 631 4399. Email: guedel@iac.unibe.ch
- ¹F. Auzel, C. R. Acad. Sci. Paris, 1016 (1966).
- ²S. M. Jacobsen and H. U. Güdel, *J. Lumin.* **43**, 125 (1989).
- ³U. Oetliker, M. J. Riley, P. S. May, and H. U. Güdel, *Coord. Chem. Rev.* **111**, 125 (1991), and references therein.
- ⁴D. R. Gamelin and H. U. Güdel, *J. Am. Chem. Soc.* **120**, 12 143 (1998).
- ⁵D. R. Gamelin and H. U. Güdel, *Inorg. Chem.* **38**, 5154 (1999).
- ⁶M. Wermuth and H. U. Güdel, *J. Am. Chem. Soc.* **121**, 10 102 (1999).
- ⁷Z. J. Kiss and R. C. Duncan, *Appl. Phys. Lett.* **5**, 200 (1964).
- ⁸V. V. Ovsyankin and P. Feofilov, *Pisma Zh. Eksp. Teor. Fiz.* **3**, 487 (1966) [*JETP Lett.* **3**, 317 (1966)].
- ⁹M. Altarelli and D. L. Dexter, *Opt. Commun.* **2**, 36 (1970).
- ¹⁰J. Ferguson, H. J. Guggenheim, and Y. Tanabe, *J. Phys. Soc. Jpn.* **21**, 692 (1966).
- ¹¹R. Valiente, O. S. Wenger, and H. U. Güdel, *Chem. Phys. Lett.* **320**, 639 (2000).
- ¹²U. Kambli and H. U. Güdel, *J. Phys. C* **17**, 4041 (1984).
- ¹³M. P. Hehlen and H. U. Güdel, *J. Chem. Phys.* **98**, 1768 (1993).
- ¹⁴J. Goodyear, G. A. Steigmann, and E. M. Ali, *Acta Crystallogr., Sect. B: Struct. Crystallogr. Cryst. Chem.* **33**, 256 (1977).
- ¹⁵G. L. McPherson and L. M. Henling, *Phys. Rev. B* **16**, 1889 (1977).
- ¹⁶R. D. Shannon, *Acta Crystallogr., Sect. A: Cryst. Phys., Diffr., Theor. Gen. Crystallogr.* **32**, 751 (1976).
- ¹⁷S. R. Lüthi, Ph.D. thesis, Bern University, 1998.
- ¹⁸M. Melamud, J. Makovsky, H. Shaked, and S. Shtrikman, *Phys. Rev. B* **3**, 821 (1971).
- ¹⁹U. Kambli and H. U. Güdel, *Inorg. Chem.* **23**, 3479 (1984).
- ²⁰G. L. McPherson, K. Talluto, and R. A. Auerbach, *Solid State Commun.* **43**, 817 (1982).
- ²¹O. S. Wenger, D. R. Gamelin, and H. U. Güdel, *J. Am. Chem. Soc.* **122**, 7408 (2000).
- ²²M. Pollnau, D. R. Gamelin, S. R. Lüthi, H. U. Güdel, and M. P. Hehlen, *Phys. Rev. B* **61**, 3337 (2000).
- ²³L. D. Livanova, I. G. Saitkulov, and A. L. Stolov, *Fiz. Tverd. Tela (Leningrad)* **11**, 599 (1969) [*Sov. Phys. Solid State* **11**, 750 (1969)].
- ²⁴F. W. Ostermayer and L. G. van Uitert, *Phys. Rev. B* **1**, 4208 (1970).
- ²⁵J. P. van der Ziel and L. G. van Uitert, *Phys. Rev.* **180**, 343 (1969).
- ²⁶J. P. van der Ziel and L. G. van Uitert, *Phys. Rev. B* **8**, 1889 (1973).
- ²⁷M. A. Aebersold, H. U. Güdel, A. Hauser, A. Furrer, H. Blank, and R. Kahn, *Phys. Rev. B* **48**, 12 723 (1993).